PHYSICAL REVIEW A **108**, 023513 (2023)

Reconfigurable valley topological QED platform for qubit operation

Junhua Dong,[1] Bingsuo Zou,[2] and Yongyou Zhang[1,*]
[1]*Beijing Key Laboratory of Nanophotonics & Ultrafine Optoelectronic Systems, School of Physics, Beijing Institute of Technology, Beijing 100081, China*
[2]*MOE & Guangxi Key Laboratory of Processing for Non-ferrous Metals and Featured Materials, School of Physical science and Technology, Guangxi University, Nanning 530004, China*

(Received 25 October 2022; accepted 26 July 2023; published 17 August 2023)

Multifarious topological crystals are extensively explored because of their unique advantages in manipulating wave transport and immunity against local perturbations. Most of them are studied, however, in feature-fixed systems and therefore, commonly have a challenge in application that requires tunability, such as quantum switches, tunable quantum routers, and quantum storage and reading. Here, we theoretically suggest a reconfigurable valley topological quantum electrodynamics (QED) platform scheme based on the honeycomb lattice of Jaynes-Cummings emitters, which can be implemented by cavity- or circuit-QED cells. Based on such a reconfigurable platform, this work first designs a tunable topological quantum router and then demonstrates how to achieve topological quantum storage and reading in theory. They both signify the remarkable potential of the suggested reconfigurable topological QED platform for qubit operation.

DOI: 10.1103/PhysRevA.108.023513

I. INTRODUCTION

Topology starting from condensed matters [1–5] has brought about great prosperities in diverse wave systems, for instance, cold atomic gases [6–8], photonics [9–11], acoustics [12], and so on. As one of the most famous topological systems, topological insulators are immune to local perturbations, exhibiting backscattering-free transport of edge states [13–15]. Recently, the blossoming of topological photonics benefits from the development of photonic crystals and metamaterials, since they can provide multifarious optical structures [16–19]. Electromagnetic waves of two vectors facilitate richer physics with respect to other classical scalar ones. In optics, topological photonics has been broadly used as a versatile platform to investigate not only fundamental nontrivial bulk and edge physics but also potential quantum techniques with topological protection, presenting short- or mid-term technological shocks in applications. The intuitive straightforward application of topological photonics exists in utilizing topologically protected edge states as robust optical waveguides [18–22] or optically isolating elements [23–25]. Though numerous systems are currently suitable for evidencing robust propagation of edge states, how to apply topology to practical application is still a trending topic, for example, topological lasers [26–29] and qubit protection [30].

Practicability and tunability require stringent conditions for topological systems. Different strategies have been explored with carefully engineered structures [31–34], involving magnetic [31,32] or external modulation [33,34]. Regretfully, most widely explored topological structures are settled after fabrication, and so are their corresponding topological properties, which, generally speaking, are not friendly to tunability and practicability. The reported tunable schemes are mainly to tune the refractive index distribution of topological structures by electric fields with electro-optical materials [35,36], magnetic fields with magnetoelastic materials [37], light irradiation with photorefractive materials [38,39], mechanical control [40], and so on [41,42]. Though these schemes demonstrate extensive potential application in controlling topological edge states, they face a difficulty in working with quantum processing, since their structures are classical in essence. The common solution is to add quantum emitters or units to them, so that the topology of classical platforms can protect or influence quantum emitters, similar to topological lasers [26–29] and topologically protected qubits [30]. These structures also face a difficulty in turning on or off the system topology. To overcome the difficulties, this work theoretically suggests a topological quantum platform by cavity-QED [43–55] or circuit-QED cells, since these cells have been achieved in experiments [56–66]. The main advantage of QED-based platforms relies upon controllable geometry and interactions. For example, artificial gauge fields and synthetic magnetic fields can be realized, respectively, in cavity arrays by trapping single atoms in cavities [67] and in circuit-QED architectures through passive circulator elements [68,69]. In addition, researchers are able to break time-reversal symmetry in lattices of microwave cavities by engineering local wave functions [70,71]. QED-based platforms are revealed as an essential landmark for the development of quantum technologies. Different from introducing artificial fields or breaking time-reversal symmetry, we here break the parity symmetry of the honeycomb lattice of Jaynes-Cummings emitters (JCEs) and suggest a reconfigurable valley topological QED platform. The potential applications of such a platform,

---

[*] yyzhang@bit.edu.cn

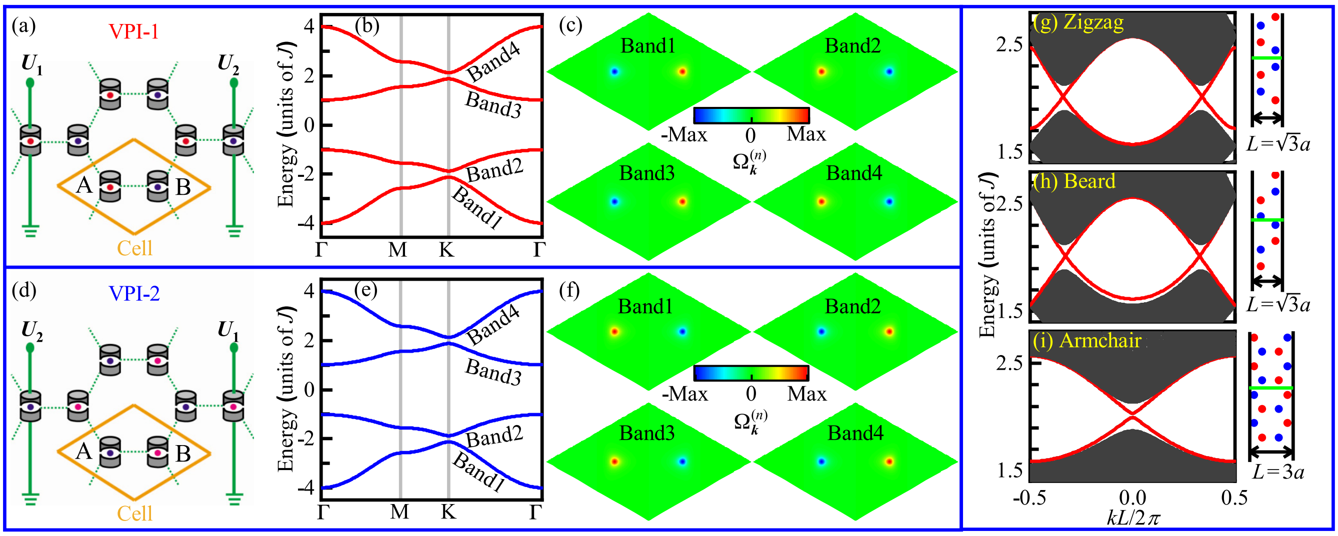

FIG. 1. Composition and properties of QED lattice. [(a) and (d)] Honeycomb cavity-QED lattices of the JCEs. The transition energies of the two-level atoms (dots) in the cativies (cylinder) depend on the external electrostatic fields [72,73]. [(b) and (e)] Corresponding band structures of the VPI-1 in (a) and the VPI-2 in (d). [(c) and (f)] Berry curvatures in the first Brillouin zone for the bands in (b) and (e). [(g)–(i)] Dispersions of the edge states on the zigzag, beard, and armchair interfaces constructed by the VPI-1 and VPI-2, see the solid green lines in the schematics, with A being the B length between the adjacent sites.

namely, topological quantum routers and quantum storage and reading, are demonstrated.

To describe the reconfigurable valley topological QED lattice, this work is organized as follows. In Sec. II, we first introduce the theoretical model for the valley QED lattice and then numerically prove the robustness of the valley edge states (VESs). Subsequently, the potential applications, i.e., topological quantum routers, storage and reading, are demonstrated in Sec. III. In Sec. IV, we discuss the feasibility of the experiments based on cavity-QED and circuit-QED unit. Finally, a brief conclusion is summarized in Sec. V.

II. MODEL

The platform model relies on the honeycomb lattice of the JCEs. Each JCE consists of a single-mode optical cavity (cylinder) and an embedded two-level system (dot), see Figs. 1(a) and 1(d). They can be implemented by cavity-QED [43–55] or circuit-QED [56–66,68,74,75] cells. Though circuit-QED is also a good choice, we here take the cavity-QED to show the model. The cylinders denote the cavities in which the red and blue dots represent the two-level atoms. The Hamiltonian of the ith JCE reads

$$\mathcal{H}_i = \tilde{\omega}_i^c \hat{c}_i^\dagger \hat{c}_i + \tfrac{1}{2}\tilde{\omega}_i^a \hat{\sigma}_i^z + \Omega_i(\hat{\sigma}_i^+ \hat{c}_i + \hat{c}_i \hat{\sigma}_i^-), \tag{1}$$

where $\tilde{\omega}_i^c = \omega_i^c - i\gamma_i^c$ ($\tilde{\omega}_i^a = \omega_i^a - i\gamma_i^a$) with cavity eigenfrequency ω_i^c and loss γ_i^c (atomic transition energy ω_i^a and loss γ_i^a), Rabi coupling Ω_i, cavity creation and annihilation operators $\hat{c}_i^\dagger$ and $\hat{c}_i$, Pauli matrix $\hat{\sigma}_i^z$, and atomic raising and lowering operators $\hat{\sigma}_i^\pm$. Summarizing $\mathcal{H}_i$ and combining the nearest-neighbor cavity-cavity couplings lead to the whole lattice Hamiltonian

$$\mathcal{H} = \sum_i \mathcal{H}_i - J\sum_{\langle ij\rangle} \hat{c}_i^\dagger \hat{c}_j. \tag{2}$$

Here, J as the unit of energies measures the photon tunneling between the two adjacent cavities and a denotes the distance between them. The atomic transition energy can be tuned by an external electric field [72,73], and so can the detuning between the cavity mode and atomic transition, $\delta_i = \omega_i^c - \omega_i^a$. The tuning way is demonstrated in Figs. 1(a) and 1(d), where the electrostatic potential applied on each JCE can be controlled independently. Without loss of generality, we take the eigenfrequencies of all cavities to be identical and as the reference point of energies, that is, $\omega_i^c \equiv 0$, and also set $\Omega_i \equiv \Omega = 2J$, $\gamma_i^c \equiv \gamma_c$, and $\gamma_i^a \equiv \gamma_a$. The detunings in sublattice A (B) of the valley photonic insulator 1 [VPI-1, Fig. 1(a)] are set to $\delta_i = 0.25J$ ($-0.25J$), opposite to those in the valley photonic insulator 2 [VPI-2, Fig. 1(d)].

The energy band of the VPI can be found by transforming $\mathcal{H}$ into the reciprocal space,

$$\begin{aligned}\mathcal{H} = {} & \sum_{\boldsymbol{k},\alpha}[\delta_\alpha \hat{\sigma}^+_{\boldsymbol{k},\alpha}\hat{\sigma}^-_{\boldsymbol{k},\alpha} + \Omega(\hat{c}^\dagger_{\boldsymbol{k},\alpha}\hat{\sigma}^-_{\boldsymbol{k},\alpha} + \hat{c}_{\boldsymbol{k},\alpha}\hat{\sigma}^+_{\boldsymbol{k},\alpha})] \\ & + \sum_{\boldsymbol{k}}\left[J\left(1 + e^{i\boldsymbol{k}\cdot\boldsymbol{a}_1} + e^{i\boldsymbol{k}\cdot\boldsymbol{a}_2}\right)\hat{c}^\dagger_{\boldsymbol{k},\mathrm{B}}\hat{c}_{\boldsymbol{k},\mathrm{A}} + \mathrm{H.c.}\right],\end{aligned} \tag{3}$$

where α denotes the sublattices A and B, $\boldsymbol{k}$ is the wave vector, and $\boldsymbol{a}_1 = (\frac{3a}{2}, \frac{\sqrt{3}a}{2})$ and $\boldsymbol{a}_2 = (\frac{3a}{2}, -\frac{\sqrt{3}a}{2})$ are lattice vectors. On the basis of $(\hat{c}^\dagger_{\boldsymbol{k},\mathrm{A}}, \hat{\sigma}^+_{\boldsymbol{k},\mathrm{A}}, \hat{c}^\dagger_{\boldsymbol{k},\mathrm{B}}, \hat{\sigma}^+_{\boldsymbol{k},\mathrm{B}})$, the Hamiltonian at $\boldsymbol{k}$, $\mathcal{H}_{\boldsymbol{k}}$, can be expressed as a 4×4 matrix,

$$\mathcal{H}_{\boldsymbol{k}} = \begin{pmatrix} 0 & \Omega & f(\boldsymbol{k}) & 0 \\ \Omega & \delta_A & 0 & 0 \\ f^*(\boldsymbol{k}) & 0 & 0 & \Omega \\ 0 & 0 & \Omega & \delta_B \end{pmatrix}, \tag{4}$$

with $f(\boldsymbol{k}) = J(1 + e^{i\boldsymbol{k}\cdot\boldsymbol{a}_1} + e^{i\boldsymbol{k}\cdot\boldsymbol{a}_2})$.

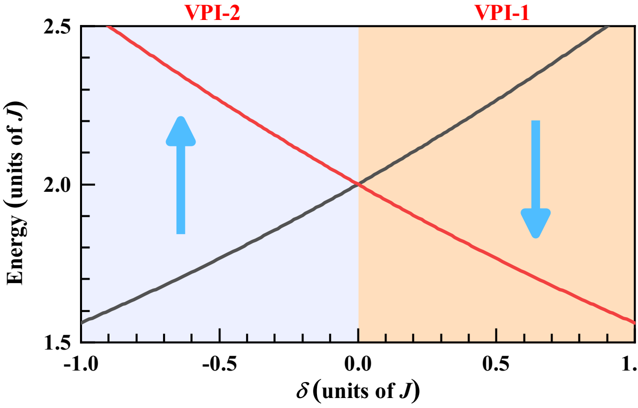

FIG. 2. Variation of the top two bands at the K point with the detuning between the cavities and atoms. Parameters: $\Omega = 2J$, $\omega_c = 0$, and $\delta_A = -\delta_B = \delta$.

Figures 1(b) and 1(e) provide the corresponding band structures, both of which hold particle-hole symmetry and gaps at K points, due to the opposite detunings in sublattices A and B. The top two bands at K points are plotted as functions of the detuning δ in Fig. 2. In view of the particle-hole symmetry, the bottom two bands are opposite with the top two. When $\delta = 0$ the gap is closed. The bands are flipped as δ changes from the negative value (VPI-2) to the positive (VPI-1). The bands are named as band 1 to band 4 from the bottom to the top and their Berry curvatures in the first Brillouin zone are plotted in Figs. 1(c) and 1(f).

The Berry curvature for the band n is defined as [76] $\Omega_{\boldsymbol{k}}^{(n)} = \nabla_{\boldsymbol{k}} \times \boldsymbol{A}_{\boldsymbol{k}}^{(n)}$, where the Berry connection $\boldsymbol{A}_{\boldsymbol{k}}^{(n)} = i\langle u_{\boldsymbol{k}}^{(n)}|\nabla_{\boldsymbol{k}}|u_{\boldsymbol{k}}^{(n)}\rangle$ and $|u_{\boldsymbol{k}}^{(n)}\rangle$ denotes the nth normalized eigenstate with the Bloch wave vector $\boldsymbol{k}$. The Berry curvatures near K and K$'$ have nonzero values, see Figs. 1(c) and 1(f), implying that the bands in Figs. 1(b) and 1(e) are nontrivial. Because the detunings in VPI-1 are opposite with those in VPI-2, the Berry curvatures in them are opposite too [see Figs. 1(c) and Fig. 1(f)], which brings about valley edge states (VESs) on their edges. The zigzag, beard, and armchair edges are demonstrated, see the right of Figs. 1(g)–1(i), where L denotes the lattice period along the edges. For all the VESs in Figs. 1(g)–1(i), only the positive energy range is focused on due to the particle-hole symmetry. The gap at the crossing point between the two branch VESs is much smaller in the zigzag and beard interfaces than in the armchair one [77]. This suggests us to use the zigzag or beard edges to operate quantum qubits, such as quantum routers and quantum storage and reading. Without loss of generality, we use the zigzag edge in this work, after all it is more familiar to researchers.

The potential application of the zigzag edge relies on the robustness of the corresponding edge states, which, however, can be influenced by losses, disorders, and noises [79]. To measure these influences, we plot the transmission of the VESs after they take the time of $0.7\tau_0$ ($\tau_0 = 2\pi/J$) to transmit the distance of $10\sqrt{3}a$ along the zigzag interface in Fig. 3. In order to calculate the transmission, the fourth-order Runge-Kutta method is applied to solve the following

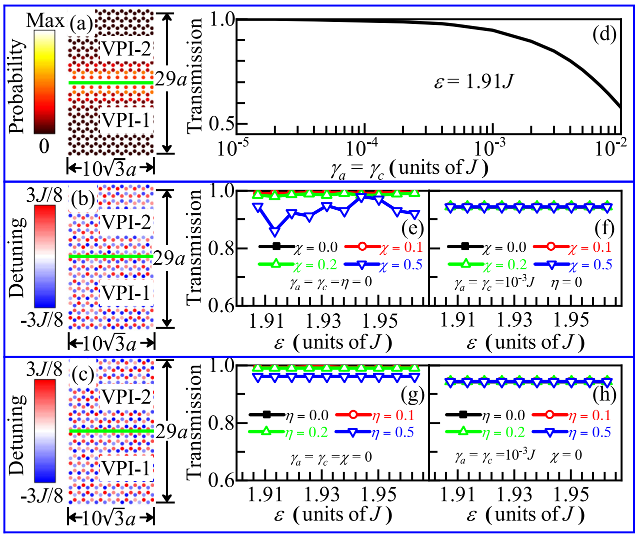

FIG. 3. Robustness of the VESs. (a) Probability distribution of the VES with the energy $\varepsilon = 1.91J$. Detuning distributions (b) for disorder strength $\chi = 0.5$ and (c) for noise strength $\eta = 0.5$. In (a)–(c), the green lines denote the zigzag edges. (d) Transmission of the VES in (a) under different cavity and atom losses (γ_c and γ_a). Transmission spectra (e) under different χ and (g) under different η without cavity or atom loss. Transmission spectra (f) under different χ and (h) under different η with cavity and atom loss $\gamma_c = \gamma_a = 10^{-3}J$. In (d)–(h), the VESs transmit the distance of $10\sqrt{3}a$ along the zigzag edge and take about the time of $0.7\tau_0$. The other parameters are the same as Figs. 1(a) and 1(d).

Schrödinger equation:

$$i\hbar\frac{\partial}{\partial t}|\psi(t)\rangle = \mathcal{H}|\psi(t)\rangle, \tag{5}$$

in the real space. The initial wave function is taken as the Gaussian wave of the VESs whose width and center energy, respectively, are $24\sqrt{3}a$ and $1.91J$. After a certain time, the initial wave will move from the incident port to the output one. The total probability received by the output port is the transmission. The probability distribution of the considered VES with the energy $\varepsilon = 1.91J$ concentrates on the zigzag interface, i.e., the transmission path, guided by the solid green line in Fig. 3(a). The transmission decreases as the atom and cavity losses increase, see Fig. 3(d). When $\gamma_a = \gamma_c$ takes $10^{-2}J$ and $10^{-3}J$, the transmissions are about 57.6% and 94.6%. For the cavity-QED experiment in Ref. [46] (circuit-QED experiment in Ref. [57]), the above losses require the cavity quality factor $Q \equiv \omega_c/\gamma_c$ approaches to 10^9 and 10^{10} (10^4 and 10^5), respectively. These values of Q satisfy the experiments, see Tables I and II.

Figures 3(e)–3(h) show the influences of disorders and noises whose relative strengths are measured by χ and η, respectively. They are introduced by changing the detunings of the JCEs,

$$\delta_i \rightarrow \delta_i \times [1 + \text{Rand}(\chi)], \quad \delta_i \rightarrow \delta_i \times [1 + \text{Rand}(\eta)], \tag{6}$$

where Rand(χ) [Rand(η)] represents a random number, evenly distributed in $(-\chi,\ \chi)$ $[(-\eta,\ \eta)]$. Rand(χ) does not change with time, while Rand(η) does, that is, all δ_i do not change with time for disorders, while do change for noises.

TABLE I. Experimental parameters for cavity-QED systems.

	$\omega_c/2\pi$	$\gamma_c/2\pi$	Q	$\omega_a/2\pi$	$\gamma_a/2\pi$	τ_a	$\Omega/2\pi$
Ref. [46]	352 THz	4 MHz	8.8×10^9	352 THz	2.6 MHz	61ns	32 MHz
Ref. [48]	385 THz	1.25 MHz	3×10^8	385 THz	6 MHz	27ns	4.5 MHz
Ref. [50]	346 THz	1.2 MHz	2×10^8	346 THz	1.69 MHz	94ns	0.92 MHz
Ref. [51]	330 THz	4.1 MHz	8×10^7	352 THz	2.6 MHz	61ns	34 MHz
Ref. [54]	384 THz	1.25 MHz	3×10^8	384 THz	–	–	11.2 MHz
Ref. [55]	384 THz	1.3 MHz	2.95×10^8	384 THz	3 MHz	53ns	11.5 MHz
Ref. [43]	21.456 GHz	0.08 KHz	2.7×10^8	21.456 GHz	–	–	–
Ref. [44]	51 GHz	0.73 KHz	7×10^7	51 GHz	5 KHz	30ms	25 KHz
Ref. [45]	51 GHz	63.8 KHz	8×10^5	51 GHz	–	–	25 KHz
Ref. [47]	21.456 GHz	0.00636 KHz	3.4×10^9	21.456 GHz	–	–	–
Ref. [53]	51 GHz	0.00123 KHz	4.15×10^{10}	51 GHz	–	–	51 KHz

Figures 3(b) and 3(c) show an example for them, respectively, with $\chi=\eta=0.5$. The largest absolute detuning, accordingly, takes the value of $0.25J\times(1+0.5)=0.375J$. To calculate the transmission of the VESs, the incident state is taken as the Gaussian pulse with the width of $24\sqrt{3}a$ and the central energy of $1.91J$. Figures 3(e) and 3(g) show the transmission spectra without any losses. They show that the transmission approximates to 1 when no disorder or noise is introduced, see the lines with square dots in them. The transmission is larger than 98% even for $\chi=0.2$ and $\eta=0.2$. When the disorder and noise are further increased to 0.5, the transmission will drop to about 0.9. As a result, the influences of disorders and noises on the system are negligible as their relative strengths are less than 20%. Figures 3(f) and 3(h) show the transmission spectra when cavity and atom losses take $\gamma_a=\gamma_c=10^{-3}J$. They demonstrate that disorder and noise show a very weak influence on the transport of the VESs, since the transmission approaches 94%, even if the strength of noise or disorder reaches 0.5. These tests tell that such a QED VPI can be used to design topologically protected quantum devices that are immune to disorders and noises. In addition, another important advantage of topological edge states compared to trivial waveguides is their immunity to local bendings [18]. Hereafter, we will take quantum routers and quantum storage and reading as examples. They may boost the application of reconfigurable topology in quantum information processing, based on the reconfigurability of the topology in cavity-QED or circuit-QED structures.

III. POTENTIAL APPLICATIONS

A. Topological quantum routers

Figure 4 demonstrates how to utilize reconfigurable topology to protect the signal routing, based on the VPIs in Figs. 1(a) and 1(d). In comparison with the reported routers [80–83], the key advantage of the scheme in Fig. 4 rests on the arbitrariness of the output-terminal position. The examined structure has 33750 sites or ideal JCEs totally, forming a hexagon, see Fig. 4.

The zigzag interfaces (see the solid green lines), whose two sides are the VPI-1 and VPI-2, can vary with time by tuning the detunings of the JCEs through the applied fields. Five cases in Fig. 4 demonstrate the time evolution of the zigzag interface from Figs. 4(a) to 4(e). Each case sustains $18\tau_0$ with $\tau_0=2\pi/J$. To see the routing, a series of the pulsed Gaussian waves (with the central frequency $\varepsilon=1.91J$, the width $24\sqrt{3}a$, and the pulse interval $6\tau_0$) are incident from the input terminal which, denoted by "In" in Fig. 4(a), remains unchanged. The state probability distributions at the five moments of $6\tau_0$, $24.1\tau_0$, $42.2\tau_0$, $60.3\tau_0$, and $78.4\tau_0$ are shown, corresponding to the five zigzag interfaces, respectively. In the first case, see Fig. 4(a), the output terminal is along the bottom left direction and thus the signal is routed to the bottom left corner. With time elapsing the output terminal successively changes from the bottom left to the top left. During this process the signal is routed to the corresponding corner. The valley topology is responsible for the routing efficiency of

TABLE II. Experimental parameters for circuit-QED systems.

	$\omega_c/2\pi$	$\gamma_c/2\pi$	Q	$\omega_a/2\pi$	$\gamma_a/2\pi$	$\gamma/2\pi$	$\gamma_\phi/2\pi$	T_1	T_2	T_2^*	$\Omega/2\pi$
Units	GHz	MHz	1	GHz	MHz	MHz	MHz	μs	μs	μs	MHz
Ref. [57]	5.7	0.25	2.28×10^4	6.9	1.9	1.95	1	0.08	0.08	–	105
Ref. [59]	7.064	43	160	7.089	0.48	0.49	0.25	0.33	0.32	–	3.5
Ref. [60]	7.804	0.769	1×10^4	5.622	0.0138	0.0179	0.002	11.5	8.9	–	–
Ref. [61]	4.25	0.12	3.5×10^7	7.9	0.01	0.016	0.011	15	10	–	4.5
Ref. [62]	7.6316	6.9	8.48×10^3	4.662	0.00187	–	–	85	–	–	–
Ref. [62]	7.6314	1.2	6.36×10^3	4.6968	0.00113	–	–	140	–	–	–
Ref. [63]	6.135	19	323	6.135	0.05	–	–	3	–	–	40
Ref. [64]	10.63	3.57	2.98×10^3	7.8693	0.005	0.006	0.0035	32	26.5	26	–
Ref. [65]	5.495	0.89	5.66×10^3	4.532	0.018	–	–	9	10	10	1.02

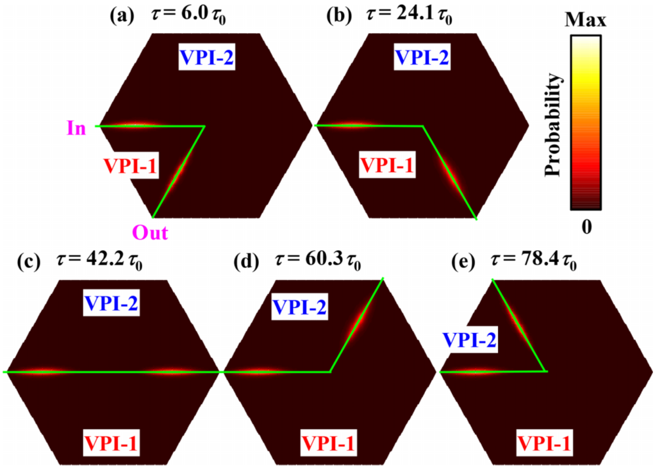

FIG. 4. Schematics for the tunable topological quantum router. The input terminal is always on the left side, while the output terminal changes with time from (a) bottom left, (b) bottom right, (c) right, (d) top right, to (e) top left, connected by the zigzag edges, see the green lines. The contour colors demonstrate the probability distributions of the incident single-photon pulse at different given times. Total 33 750 JCEs are considered and the band parameters are the same as Figs. 1(a) and 1(d).

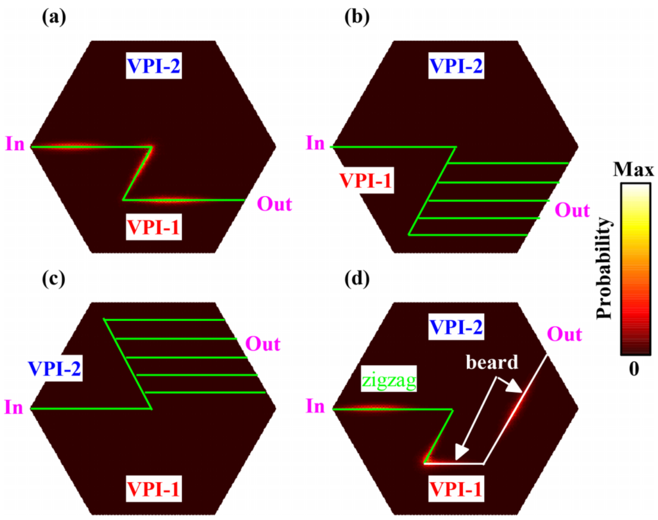

FIG. 5. Topological routers with arbitrary adjustable path. The green lines in all panels denote the zigzag edges. The beard edges in (d) are denoted by two arrows. Parameters are the same as those in the Fig. 4.

∼100% for all cases, because of the robustness against local defects (such as waveguide bending), while the transmission for the trivial waveguide strongly depends on local defects [18,76].

When the losses $\gamma_a = \gamma_c = 10^{-3}J$ are introduced, the transmission loss and traveling time are about 10.5% and $1.4\tau_0$, respectively, when the path length is set to $20\sqrt{3}a$. Once the path length decreases to $10\sqrt{3}a$, the transmission loss is about 5.4%, and the corresponding traveling time is about $0.7\tau_0$. This traveling time is far less than the dephasing time $T_1 \equiv \frac{1}{\gamma_a} \approx 160\tau_0$, satisfying the cavity-QED unit in Ref. [46] and the circuit-QED unit in Ref. [57] (see Sec. IV for details). This indicates that such a reconfigurable VPI can serve as a topological quantum router (see video I in Ref. [78]).

The transport of the VESs can be adjusted by the path control in any direction with the topological path bent multiple times. Such an example in Fig. 5(a) shows the probability distribution of the directed VES on the curved path. Its transport is topologically protected and immune to the waveguide bending. Figures 5(b) and 5(c) show the path adjustability. One can arbitrarily adjust the position of the output terminal at will. In addition, different interfaces in this designed structure can be mixed, see Fig. 5(d), where mixing the zigzag and beard edges does not disturb the VES transport. These adjustabilities together with the valley topology are beneficial for the application of the suggested topological QED platform.

In Figs. 4 and 5, 33 500 sites are used for demonstrating the quantum router, which does not mean that one must use so many lattices. The size of lattice is mainly determined by the VES width normal to the topological path. Our numerical calculations indicate that such a width is about 16 sites, namely, $11a$, see Fig. 6, where the zigzag interface is used. As a result, the path width had better contain more than 40 sites to form a perfect VES, namely, $29a$, see Fig. 6. Therefore, the total number of the required sites is proportional to the path length, that is, the minimum number of cavities is about $40L/\sqrt{3}a$, where L denotes the path length. In Fig. 6, the minimum number of sites is about 400, if the path length takes $10\sqrt{3}a$.

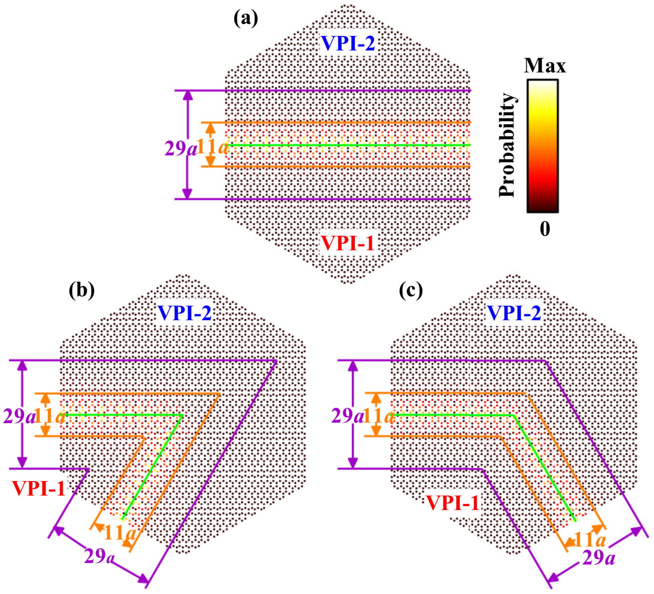

FIG. 6. Probability distribution of the VESs on zigzag interfaces with different bending angles: (a) 0°, (b) 120°, and (c) 60°. The green lines present the zigzag edges. The orange lines are the broadening width of the VES normal to the edge. The purple lines demonstrate the path width that required for a perfect VES. Total 3120 JCEs are used and the band parameters are the same as Figs. 1(a) and 1(d) in the main text.

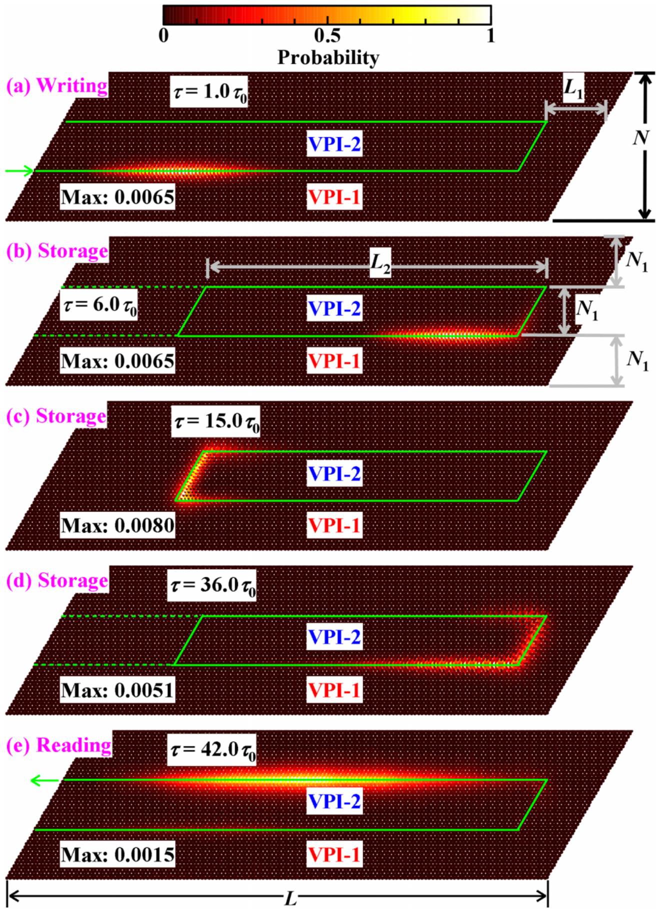

FIG. 7. Schematic for topological quantum storage and reading. (a) Writing the quantum state into the opened topological edges when $\tau \in (0\tau_0, 6\tau_0)$. [(b)–(d)] Storage of the quantum state within the closed topological edge when $\tau \in [6\tau_0, 36\tau_0]$. (e) Reading the quantum state with the opened topological edge when $\tau \in (36\tau_0, 48\tau_0)$. The green lines represent the transmission paths and the arrows denote the input and output ports. The contour colors show the probability distributions of the VES at different given moments. The maximum values of probabilities are denoted by "Max" in each panel. Total 14 400 JCEs are considered as $L = 150\sqrt{3}a$, $N = 71a$, $L_1 = 16\sqrt{3}a$, $L_2 = 94\sqrt{3}a$, $N_1 = 23a$, and the band parameters are the same as Figs. 1(a) and 1(d).

B. Topological quantum storage and reading

As two key techniques in quantum informatics, quantum storage and reading always intrigue researchers, for which numerous schemes have been proposed [84–89]. Without topology, conventional methods commonly suffer disturbance of system disorder and imperfection. Here, we use the VESs to realize the writing, storage and reading of quantum states, which are immune to system disorders and path bending, see Figs. 3(e) and 4.

The suggested architecture is shown in Fig. 7, varying with time. It holds the open zigzag interface as time $\tau \in (0,\ 6\tau_0) \cup (36\tau_0,\ 48\tau_0)$, see Figs. 7(a) and 7(e) and the closed one as $\tau \in [6\tau_0,\ 36\tau_0]$, see Figs. 7(b)–7(d). During the time interval of $(0,\ 6\tau_0)$, the Gaussian state (with the width $24\sqrt{3}a$ and the central frequency $\varepsilon = 1.91J$) is incident from the lower left terminal, see the green arrow in Fig. 7(a), behaving as the writing of the quantum qubit. When the time arrives at $\tau = 6\tau_0$, the quantum state moves to the position demonstrated in Fig. 7(b) and simultaneously, the open zigzag interface is changed to the closed one. As a result, the quantum state is stored into the closed topological interface during the time interval of $[6\tau_0,\ 36\tau_0]$, see Fig. 7(c) with $\tau = 15\tau_0$. If this storage interval increases one can expect a long-time storage of the quantum state. During the storage interval of $[6\tau_0,\ 36\tau_0]$, the quantum state roughly runs two loops along the closed topological interface. The closed interface is opened at $\tau = 36\tau_0$ and the corresponding spatial probability distribution of the quantum state is shown in Fig. 7(d). With time elapsing the quantum state moves to the output terminal, behaving as the reading of the quantum state, see Fig. 7(e). The procedures of writing, storage, and reading are demonstrated in videos II and III in Ref. [78].

Here, we discuss the possibility of experimental implementation. We consider a case with the circumference of the closed path being $40\sqrt{3}a$. The corresponding storage time is about $2.8\tau_0$ as the VES travels around the closed path once, corresponding to the storage loss of 20.0% where $\gamma_a = \gamma_c = 10^{-3}J$ are adopted. When the VES travels around the closed path twice, the above storage time are doubled, but with a higher loss of 36%. These values of loss are acceptable in experiments and the operation time is far less than T_1. Such a storage time measured by the oscillation period of the cavity mode $\tau_c = 2\pi/\omega_c$ would be $6.2 \times 10^7 \tau_c \approx 176$ ns for cavity-QED experiment in Ref. [46] and be $305\tau_c \approx 61$ ns for circuit-QED experiment in Ref. [57], see Sec. IV for details.

IV. FEASIBILITY ANALYSIS OF EXPERIMENTS

In this section, we will discuss the experimental implementation of the scheme using the cavity- and circuit-QED platforms, respectively. In view of theoretical study, we favor them equally. However, experimentalists may have a different favor in state-of-the-art laboratories, after all the two platforms have their own advantages. The cavity-QED platform is the most basic implementation method. The cavity-QED system can suppress the decoherence between the system and surrounding environment to a large extent as long as the cavity has a sufficiently high quality factor. For the circuit-QED platform, not only the energy level, but also other parameters of the artificial atom can be controlled easily, since the qubit can be regarded as an artificial atom. The circuit-QED system has been comprehensively researched and greatly promoted the cavity-QED.

A. Cavity-QED platforms

The present section discusses the possible cavity-QED platforms in experiments and the key parameter values of some typical schemes, referred to the reported experimental parameters in Table I. The meanings of the parameters are ω_c is the cavity frequency, γ_c is the cavity loss, $Q = \omega_c/\gamma_c$ is the cavity quality factor, ω_a represents the atom transition frequency, γ_a is the loss of atom, τ_a is the atom lifetime, and Ω is the Rabi coupling between the atom and cavity. According to Fig. 3(d), the transmission loss of the VESs is about 42.4% when $\gamma_a = \gamma_c = 0.01J$, as they transmit the

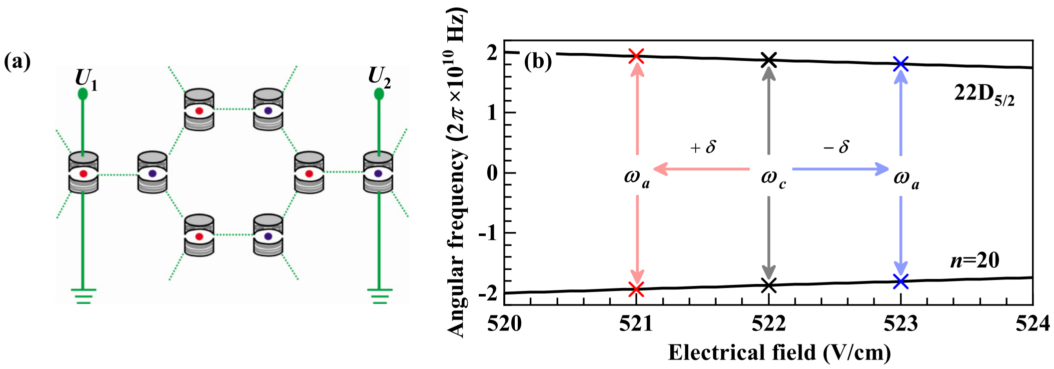

FIG. 8. (a) Honeycomb cavity-QED lattice of the JCEs. (b) Concerned energy levels for ^{87}Rb in the electrostatic field, refer to Ref. [72] for details. As an example, we assume $\omega_c \approx 2\pi\times37$ GHz, the two atom transition energies $\omega_1 = \omega_c + \delta$ and $\omega_2 = \omega_c - \delta$ with $\delta \approx 2\pi\times1.3$ GHz, the hopping $J \approx 25.5$ KHz, the Rabi coupling $\Omega \approx 51$ KHz [53], the cavity loss $\gamma_c = 2\pi\times0.025$ KHz, leading the corresponding cavity quantity factor $Q = 1.48\times10^9$. These values of parameters satisfy the experimental conditions in Ref. [53], see the last row of Table I. ω_1 and ω_2 correspond to the electrostatic fields of 521 and 523 V/cm, respectively.

distance of $10\sqrt{3}a$ along the zigzag edge and takes the time of about $0.7\tau_0$. Once we adopt $\gamma_a = \gamma_c = 0.001J$, the loss of the VESs decreases to about 5.4%.

Next, we will compare these values of parameters in our model with those in the current cavity-QED experiments. In the optical frequency, the first row in Table I is taken as an example [46], that is, the cavity frequency $\omega_c = 2\pi\times352$ THz and the Rabi coupling $\Omega = 2\pi\times32$ MHz between the cavity and the atom, leading to $J = 2\pi\times16$ MHz and $\omega_c = 2.2\times10^7 J$. Thus, the cavity quality factor Q is about 2.2×10^9 or 2.2×10^{10}, both close to the experimental value of 8.8×10^9, when we set γ_c to be $0.01J$ or $0.001J$ in our model. If considering the experimental conditions in the microwave frequency in the last row of Table I [53], one will also find that our model is available for the cavity-QED experiments. Most of these atoms are circular Rydberg atoms and have a long radiative lifetime (about 30 ms) [90], which makes atomic relaxation negligible during the atom transit time across the apparatus.

We here give a cavity-QED experimental scheme for our proposals. It relies on the honeycomb lattice of the JCEs. Each JCE consists of a cavity and an embedded Rydberg atom, for example, a ^{87}Rb is placed at the center of the cavity. A pair of parallel plates with an imposed voltage difference of U is applied to generate an electrostatic field at the position of atom, inducing the dc Stark shifts of Rydberg levels, see Fig. 8(a). The variations of the two concerned Rydberg levels of ^{87}Rb with the external electrostatic field are plotted in Fig. 8(b). In such a case, the parameters can be adopted as following: $\delta \approx 2\pi\times1.3$ GHz, $J \approx 2\pi\times25.2$ KHz, and $\Omega = 2\pi\times51$ KHz, the corresponding eigenfrequency of cavities $\omega_c \approx 2\pi\times(32\text{–}41)$ GHz. The cavity can tolerance the loss of $\gamma_c = 2\pi\times0.025$ KHz, leading to the corresponding cavity quantity factor $Q = (1.28\text{–}1.64)\times10^9$. The applied electric fields are about 520–550 V/cm. These experimental parameters are possible in the cavity-QED platform [46].

B. Circuit-QED platforms

Circuit-QED is another practical implementation for such a reconfigurable topological platform. Instead, the typical circuit QED experiments work with resonators in the range of 5–15 GHz. In Table II, γ_a is the energy decay for the qubit, $\gamma = \gamma_a/2 + \gamma_\phi$ is the decoherence rate with the pure dephasing rate γ_ϕ, $T_1 = 1/\gamma_a$ is the relaxation time, $T_2 = 1/\gamma$ is the dephasing time corresponding to the intrinsic dephasing of the qubit (homogeneous broadening), and T_2^* is the dephasing time corresponding to the inhomogeneous broadening. The meanings of other parameters are the same as those in Table I. For the transmon qubit, it is immune to $1/\text{f}$ charge noise and is nearly homogeneously broadened, implying $T_2 \approx T_2^*$ [84].

In the following, these values of parameters in our model will be compared with those in the current circuit-QED experiments. As an example, we take the experimental parameters in the first row of Table II [57]. Correspondingly, the cavity frequency $\omega_c = 2\pi\times5.7$ GHz and the Rabi coupling between the cavity and the artificial atom $\Omega = 2\pi\times105$ MHz, leading to $J = 2\pi\times52.5$ MHz and $\omega_c = 109J$ in our model. Consequently, the quality factor required is about 10^4 or 10^5, when we adopt $\gamma_c = 0.01J$ or $\gamma_c = 0.001J$. In the first row of Table II, the Q in experiments can reach 10^4. Especially, the fourth row of Table II indicates that the Q in experiments can be larger than 10^7. In Fig. 3(d), the VESs take the time of $0.7\tau_0$ to transmit the distance of $10\sqrt{3}a$, in which the transmission is about 94.6% as $\gamma_a = \gamma_c = 0.001J$. These parameters lead to $0.7\tau_0 \ll T_1 \approx 160\tau_0$ (we hereafter will always use T_1 for comparison since $T_1 < T_2 \approx T_2^*$), which indicates that the quantum operation can commonly be completed during the time of T_1. These discussions are also available for the experimental values in the rest cases of Table II.

Based on these analyses, we here propose the following experimental circuit-QED platform. For the circuit-QED platform, the key element is the cavity resonator coupled to a superconducting qubit [68,74,75]. In Fig. 9(a), the cylinders denote the cavity resonators and the red and blue dots represent the superconducting transmon qubits. The model of the transmon qubit is shown in Fig. 9(b), whose frequency can be tuned by the external magnetic flux Φ, see Fig. 9(c). The transmon consists of two superconducting islands connected by two Josephson junctions in parallel, which allows the effective Josephson energy to be tuned by an external magnetic field, $E_J = E_J^{\max}|\cos(\pi\Phi/\Phi_0)|$, where $E_J^{\max}$ is the maximum

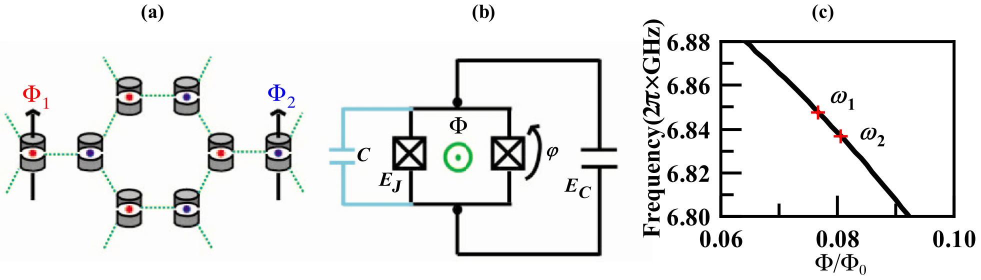

FIG. 9. (a) Honeycomb circuit-QED lattice of the JCEs. The cylinders denote the cavity resonators. The red and blue dots represent the superconducting transmon qubits, whose frequencies can be tuned by the external magnetic field. (b) Model of the transmon qubit that consists of two superconducting islands connected by a Josephson tunnel junction and a large capacitance. The tunneling of Cooper pairs between the two islands is governed by the charging energy E_C, the Josephson energy E_J, and the conjugate phase φ. (c) Concerned energy spectra for the transmon qubits as a function of magnetic flux Φ, referred to Ref. [74] for details. As an example, we choose the cavity resonator frequency to be $\omega_c \approx 2\pi \times 6.84$ GHz, and the frequency for $\omega_1 = 2\pi \times 6.8459$ GHz and $\omega_2 = 2\pi \times 6.8341$ GHz with the magnetic flux of $0.0815\Phi_0$ and $0.0774\Phi_0$ (Φ_0 is the flux quantum), the hopping strength between the adjacent cavities to be $J = 2\pi \times 23.5$ MHz, and the Rabi coupling to be $2\pi \times 47$ MHz. And the cavity and qubit loss γ_c and γ_a can be $2\pi \times 0.0235$ MHz, which lead to the cavity quantity factor Q is about 3×10^5.

Josephson energies, Φ is the magnetic flux and Φ_0 is the flux quantum. In the limit of high E_J/E_C, the qubit frequency follows the asymptotic form $\omega_a = \sqrt{8E_J E_C} - E_C$. Changing the magnetic field allows one to change E_J, and so does the atom frequency ω_a, see Fig. 9(c). The tunneling of Cooper pairs between two islands is governed by the charging energy E_C, the Josephson energy E_J, and the conjugate phase φ. The coupling strength between the adjacent cavity resonators can be tuned by mutual capacitance between their ends [68].

In such a case, according to Ref. [74], the parameters can be adopted as following: the interaction strength Ω between the superconducting qubit and cavity resonator is about $\Omega \approx 2\pi \times 47$ MHz and the superconducting qubit frequency is about in the range of $2\pi \times (4.5, 7)$ GHz. These experimental data suggest us to take the cavity resonator frequency to be $\omega_c \approx 2\pi \times 6.84$ GHz [74] and the detuning between the cavity resonators and superconducting qubits to be $\delta \approx 2\pi \times 5.9$ MHz. The superconducting qubits corresponding to the red and blue dots have the frequencies of $2\pi \times 6.8459$ GHz and $2\pi \times 6.8341$ GHz with the magnetic flux $\Phi = 0.0774\Phi_0$ and $\Phi = 0.0815\Phi_0$, respectively, see Fig. 9(c). The corresponding value of the hopping strength between the adjacent cavity resonators can be taken as about $2\pi \times 23.5$ MHz. The cavity and qubit can tolerate the loss of $2\pi \times 0.0235$ MHz, which lead to the cavity quantity factor Q is about 3×10^5.

We also point out that the scheme still has a challenge in how to effectively group hundreds or thousands of cavity- or circuit-QED cells into a honeycomb lattice, though single cavity- and circuit-QED cell have been achieved in the state-of-art experiments with high quality. With the development of advanced micro/nanofabrication techniques, we hope that such a controllable valley topological QED lattice can be achieved in the future.

V. CONCLUSION

In summary, this work theoretically suggests a reconfigurable valley topological QED platform for qubit operation based on either cavity- or circuit-QED cell. With it, we demonstrate a tunable topological quantum router and a topological quantum storage and reading. The numerical verification confirms that they have excellent performance, so that the suggested reconfigurable valley topological quantum platform may have wide application in quantum informatics.

Though the required conditions of the platform are satisfied by the current cavity- and circuit-QED techniques, it also faces a challenge in how to integrate many QED cells to form a lattice. We expect this challenge can be overcome in future, after all it is not a fundamental barrier in principle. Additionally, how to accurately analyze the transport of multi-particle quantum states in such a topological platform is still an open question and the related phenomena brought by the system nonlinearity may open the door to new applications [51,91].

ACKNOWLEDGMENTS

This work is supported by the National Natural Science Foundation of China (Grant No. 12074037) and the Bagui scholar fund of Guangxi province.

---

[1] K. v. Klitzing, G. Dorda, and M. Pepper, Phys. Rev. Lett. **45**, 494 (1980).
[2] F. D. M. Haldane, Phys. Rev. Lett. **61**, 2015 (1988).
[3] C. L. Kane and E. J. Mele, Phys. Rev. Lett. **95**, 226801 (2005).
[4] L. Fu, C. L. Kane, and E. J. Mele, Phys. Rev. Lett. **98**, 106803 (2007).
[5] H. Zhang, C.-X. Liu, X.-L. Qi, X. Dai, Z. Fang, and S.-C. Zhang, Nat. Phys. **5**, 438 (2009).
[6] N. R. Cooper, Adv. Phys. **57**, 539 (2008).
[7] N. Goldman, G. Juzeliūnas, P. Öhberg, and I. B. Spielman, Rep. Prog. Phys. **77**, 126401 (2014).
[8] N. Goldman, J. C. Budich, and P. Zoller, Nat. Phys. **12**, 639 (2016).

[9] L. Lu, J. D. Joannopoulos, and M. Soljačić, Nat. Photon. **8**, 821 (2014).

[10] B.-Y. Xie, H.-F. Wang, X.-Y. Zhu, M.-H. Lu, Z. D. Wang, and Y.-F. Chen, Opt. Express **26**, 24531 (2018).

[11] T. Ozawa, H. M. Price, A. Amo, N. Goldman, M. Hafezi, L. Lu, M. C. Rechtsman, D. Schuster, J. Simon, O. Zilberberg, and I. Carusotto, Rev. Mod. Phys. **91**, 015006 (2019).

[12] Z. Yang, F. Gao, X. Shi, X. Lin, Z. Gao, Y. Chong, and B. Zhang, Phys. Rev. Lett. **114**, 114301 (2015).

[13] X. Ao, Z. Lin, and C. T. Chan, Phys. Rev. B **80**, 033105 (2009).

[14] M. Hafezi, S. Mittal, J. Fan, A. Migdall, and J. M. Taylor, Nat. Photon. **7**, 1001 (2013).

[15] J.-W. Dong, X.-D. Chen, H. Zhu, Y. Wang, and X. Zhang, Nat. Mater. **16**, 298 (2017).

[16] Y. Yang, Y. F. Xu, T. Xu, H.-X. Wang, J.-H. Jiang, X. Hu, and Z. H. Hang, Phys. Rev. Lett. **120**, 217401 (2018).

[17] X.-D. Chen, F.-L. Shi, H. Liu, J.-C. Lu, W.-M. Deng, J.-Y. Dai, Q. Cheng, and J.-W. Dong, Phys. Rev. Appl. **10**, 044002 (2018).

[18] J. Dong, B. Zou, and Y. Zhang, Appl. Phys. Lett. **119**, 251101 (2021).

[19] J. Dong, Q. Hu, C.-Y. Ji, B. Zou, and Y. Zhang, New J. Phys. **23**, 113025 (2021).

[20] Z. Wang, Y. D. Chong, J. D. Joannopoulos, and M. Soljačić, Phys. Rev. Lett. **100**, 013905 (2008).

[21] C. He, X.-L. Chen, M.-H. Lu, X.-F. Li, W.-W. Wan, X.-S. Qian, R.-C. Yin, and Y.-F. Chen, Appl. Phys. Lett. **96**, 111111 (2010).

[22] Y. Yang, Y. Poo, R.-X. Wu, Y. Gu, and P. Chen, Appl. Phys. Lett. **102**, 231113 (2013).

[23] Z. Yu and S. Fan, Nat. Photon. **3**, 91 (2009).

[24] T. Ozawa, H. M. Price, N. Goldman, O. Zilberberg, and I. Carusotto, Phys. Rev. A **93**, 043827 (2016).

[25] X. Zhou, Y. Wang, D. Leykam, and Y. D. Chong, New J. Phys. **19**, 095002 (2017).

[26] L. Pilozzi and C. Conti, Phys. Rev. B **93**, 195317 (2016).

[27] B. Bahari, A. Ndao, F. Vallini, A. E. Amili, Y. Fainman, and B. Kanté, Science **358**, 636 (2017).

[28] P. St-Jean, V. Goblot, E. Galopin, A. Lemaître, T. Ozawa, L. Le Gratiet, I. Sagnes, J. Bloch, and A. Amo, Nat. Photon. **11**, 651 (2017).

[29] M. Parto, S. Wittek, H. Hodaei, G. Harari, M. A. Bandres, J. Ren, M. C. Rechtsman, M. Segev, D. N. Christodoulides, and M. Khajavikhan, Phys. Rev. Lett. **120**, 113901 (2018).

[30] B. Douçot and L. B. Ioffe, Rep. Prog. Phys. **75**, 072001 (2012).

[31] F. D. M. Haldane and S. Raghu, Phys. Rev. Lett. **100**, 013904 (2008).

[32] S. Raghu and F. D. M. Haldane, Phys. Rev. A **78**, 033834 (2008).

[33] N. A. Estep, D. L. Sounas, J. Soric, and A. Alù, Nat. Phys. **10**, 923 (2014).

[34] T. Ma, A. B. Khanikaev, S. H. Mousavi, and G. Shvets, Phys. Rev. Lett. **114**, 127401 (2015).

[35] M. I. Shalaev, S. Desnavi, W. Walasik, and N. M. Litchinitser, New J. Phys. **20**, 023040 (2018).

[36] W. Hu, J. Hu, S. Wen, and Y. Xiang, Opt. Lett. **46**, 2589 (2021).

[37] J.-X. Fu, R.-J. Liu, and Z.-Y. Li, Europhys. Lett. **89**, 64003 (2010).

[38] D. A. Dobrykh, A. V. Yulin, A. P. Slobozhanyuk, A. N. Poddubny, and Y. S. Kivshar, Phys. Rev. Lett. **121**, 163901 (2018).

[39] M. I. Shalaev, W. Walasik, and N. M. Litchinitser, Optica **6**, 839 (2019).

[40] E. Saei Ghareh Naz, I. C. Fulga, L. Ma, O. G. Schmidt, and J. van den Brink, Phys. Rev. A **98**, 033830 (2018).

[41] C. Li, X. Hu, W. Gao, Y. Ao, S. Chu, H. Yang, and Q. Gong, Adv. Opt. Mater. **6**, 1701071 (2018).

[42] T. Cao, L. Fang, Y. Cao, N. Li, Z. Fan, and Z. Tao, Sci. Bull. **64**, 814 (2019).

[43] G. Rempe, H. Walther, and N. Klein, Phys. Rev. Lett. **58**, 353 (1987).

[44] M. Brune, F. Schmidt-Kaler, A. Maali, J. Dreyer, E. Hagley, J. M. Raimond, and S. Haroche, Phys. Rev. Lett. **76**, 1800 (1996).

[45] M. Brune, P. Nussenzveig, F. Schmidt-Kaler, F. Bernardot, A. Maali, J. M. Raimond, and S. Haroche, Phys. Rev. Lett. **72**, 3339 (1994).

[46] J. Ye, D. W. Vernooy, and H. J. Kimble, Phys. Rev. Lett. **83**, 4987 (1999).

[47] B. T. H. Varcoe, S. Brattke, M. Weidinger, and H. Walther, Nature (London) **403**, 743 (2000).

[48] M. Hennrich, T. Legero, A. Kuhn, and G. Rempe, Phys. Rev. Lett. **85**, 4872 (2000).

[49] C. J. Hood, T. W. Lynn, A. C. Doherty, A. S. Parkins, and H. J. Kimble, Science **287**, 1447 (2000).

[50] M. Keller, B. Lange, K. Hayasaka, W. Lange, and H. Walther, Nature (London) **431**, 1075 (2004).

[51] K. M. Birnbaum, A. Boca, R. Miller, A. D. Boozer, T. E. Northup, and H. J. Kimble, Nature (London) **436**, 87 (2005).

[52] T. Aoki, B. Dayan, E. Wilcut, W. P. Bowen, A. S. Parkins, T. J. Kippenberg, K. J. Vahala, and H. J. Kimble, Nature (London) **443**, 671 (2006).

[53] S. Gleyzes, S. Kuhr, C. Guerlin, J. Bernu, S. Deléglise, U. Busk Hoff, M. Brune, J.-M. Raimond, and S. Haroche, Nature (London) **446**, 297 (2007).

[54] I. Schuster, A. Kubanek, A. Fuhrmanek, T. Puppe, P. W. H. Pinkse, and G. Rempe, Nat. Phys. **4**, 382 (2008).

[55] A. Kubanek, A. Ourjoumtsev, I. Schuster, M. Koch, P. W. H. Pinkse, K. Murr, and G. Rempe, Phys. Rev. Lett. **101**, 203602 (2008).

[56] Y. Makhlin, G. Schön, and A. Shnirman, Rev. Mod. Phys. **73**, 357 (2001).

[57] D. I. Schuster, A. A. Houck, J. A. Schreier, A. Wallraff, J. M. Gambetta, A. Blais, L. Frunzio, J. Majer, B. Johnson, M. H. Devoret, S. M. Girvin, and R. J. Schoelkopf, Nature (London) **445**, 515 (2007).

[58] R. J. Schoelkopf and S. M. Girvin, Nature (London) **451**, 664 (2008).

[59] J. A. Mlynek, A. A. Abdumalikov, C. Eichler, and A. Wallraff, Nat. Commun. **5**, 5186 (2014).

[60] L. Bretheau, P. Campagne-Ibarcq, E. Flurin, F. Mallet, and B. Huard, Science **348**, 776 (2015).

[61] M. Reagor, W. Pfaff, C. Axline, R. W. Heeres, N. Ofek, K. Sliwa, E. Holland, C. Wang, J. Blumoff, K. Chou, M. J. Hatridge, L. Frunzio, M. H. Devoret, L. Jiang, and R. J. Schoelkopf, Phys. Rev. B **94**, 014506 (2016).

[62] A. Narla, S. Shankar, M. Hatridge, Z. Leghtas, K. M. Sliwa, E. Zalys-Geller, S. O. Mundhada, W. Pfaff, L. Frunzio, R. J. Schoelkopf, and M. H. Devoret, Phys. Rev. X **6**, 031036 (2016).

[63] J.-C. Besse, S. Gasparinetti, M. C. Collodo, T. Walter, P. Kurpiers, M. Pechal, C. Eichler, and A. Wallraff, Phys. Rev. X **8**, 021003 (2018).
[64] S. Kono, K. Koshino, Y. Tabuchi, A. Noguchi, and Y. Nakamura, Nat. Phys. **14**, 546 (2018).
[65] R. Lescanne, S. Deléglise, E. Albertinale, U. Réglade, T. Capelle, E. Ivanov, T. Jacqmin, Z. Leghtas, and E. Flurin, Phys. Rev. X **10**, 021038 (2020).
[66] A. Blais, A. L. Grimsmo, S. M. Girvin, and A. Wallraff, Rev. Mod. Phys. **93**, 025005 (2021).
[67] J. Cho, D. G. Angelakis, and S. Bose, Phys. Rev. Lett. **101**, 246809 (2008).
[68] J. Koch, A. A. Houck, K. L. Hur, and S. M. Girvin, Phys. Rev. A **82**, 043811 (2010).
[69] W. L. Yang, Z.-q. Yin, Z. X. Chen, S.-P. Kou, M. Feng, and C. H. Oh, Phys. Rev. A **86**, 012307 (2012).
[70] B. M. Anderson, R. Ma, C. Owens, D. I. Schuster, and J. Simon, Phys. Rev. X **6**, 041043 (2016).
[71] C. Owens, A. LaChapelle, B. Saxberg, B. M. Anderson, R. Ma, J. Simon, and D. I. Schuster, Phys. Rev. A **97**, 013818 (2018).
[72] D. Yu, A. Landra, M. M. Valado, C. Hufnagel, L. C. Kwek, L. Amico, and R. Dumke, Phys. Rev. A **94**, 062301 (2016).
[73] C. S. Adams, J. D. Pritchard, and J. P. Shaffer, J. Phys. B: At. Mol. Opt. Phys. **53**, 012002 (2019).
[74] J. A. Schreier, A. A. Houck, J. Koch, D. I. Schuster, B. R. Johnson, J. M. Chow, J. M. Gambetta, J. Majer, L. Frunzio, M. H. Devoret, S. M. Girvin, and R. J. Schoelkopf, Phys. Rev. B **77**, 180502(R) (2008).
[75] A. A. Houck, H. E. Türeci, and J. Koch, Nat. Phys. **8**, 292 (2012).
[76] C.-Y. Ji, Y. Zhang, B. Zou, and Y. Yao, Phys. Rev. A **103**, 023512 (2021).
[77] T. Kariyado and X. Hu, Sci. Rep. **7**, 16515 (2017).
[78] See Supplemental Material at http://link.aps.org/supplemental/10.1103/PhysRevA.108.023513 for Video I: A topological quantum router. Video II: The procedures of quantum writing and reading. Video III: The procedures of quantum writing, storage, and reading.
[79] H. Choi, D. Zhu, Y. Yoon, and D. Englund, Phys. Rev. Lett. **122**, 183602 (2019).
[80] I.-C. Hoi, C. M. Wilson, G. Johansson, T. Palomaki, B. Peropadre, and P. Delsing, Phys. Rev. Lett. **107**, 073601 (2011).
[81] L. Zhou, L.-P. Yang, Y. Li, and C. P. Sun, Phys. Rev. Lett. **111**, 103604 (2013).
[82] K. Fang, M. H. Matheny, X. Luan, and O. Painter, Nat. Photon. **10**, 489 (2016).
[83] M. Pechal, J.-C. Besse, M. Mondal, M. Oppliger, S. Gasparinetti, and A. Wallraff, Phys. Rev. Appl. **6**, 024009 (2016).
[84] J. Koch, T. M. Yu, J. Gambetta, A. A. Houck, D. I. Schuster, J. Majer, A. Blais, M. H. Devoret, S. M. Girvin, and R. J. Schoelkopf, Phys. Rev. A **76**, 042319 (2007).
[85] Y. Tanguy, T. Ackemann, W. J. Firth, and R. Jäger, Phys. Rev. Lett. **100**, 013907 (2008).
[86] F. Leo, S. Coen, P. Kockaert, S.-P. Gorza, P. Emplit, and M. Haelterman, Nat. Photon. **4**, 471 (2010).
[87] T. Herr, V. Brasch, J. D. Jost, C. Y. Wang, N. M. Kondratiev, M. L. Gorodetsky, and T. J. Kippenberg, Nat. Photon. **8**, 145 (2014).
[88] M. Pang, W. He, X. Jiang, and P. S. J. Russell, Nat. Photon. **10**, 454 (2016).
[89] C. E. Bradley, J. Randall, M. H. Abobeih, R. C. Berrevoets, M. J. Degen, M. A. Bakker, M. Markham, D. J. Twitchen, and T. H. Taminiau, Phys. Rev. X **9**, 031045 (2019).
[90] J. Raimond, M. Brune, and S. Haroche, Rev. Mod. Phys. **73**, 565 (2001).
[91] H. Choi, M. Heuck, and D. Englund, Phys. Rev. Lett. **118**, 223605 (2017).